Deciphering modes of long-range energy transfer in perovskite crystals using confocal excitation and wide-field fluorescence spectral imaging

Methods and Applications in Fluorescence

PAPER

RECEIVED
1 June 2022

REVISED
25 August 2022

ACCEPTED FOR PUBLICATION
5 September 2022

PUBLISHED
16 September 2022

Deciphering modes of long-range energy transfer in perovskite crystals using confocal excitation and wide-field fluorescence spectral imaging

Tejmani Behera , Nithin Pathoor , Rajat Mukherjee and Arindam Chowdhury*

Department of chemistry, Indian Institute of Technology Bombay, Powai, Mumbai, India
* Author to whom any correspondence should be addressed.

E-mail: arindam@chem.iitb.ac.in

Keywords: point excitation, carrier diffusion, synchronous intermittency, photon recycling, transient defects

Supplementary material for this article is available online

Abstract

Excitation energy migration beyond mesoscale is of contemporary interest for both solar photovoltaic and light-emissive devices, especially in context of organometal halide perovskites (OMHPs) which have been shown to have very long (charge carrier) diffusion lengths. While understanding the energy propagation pathways in OMHPs is crucial for further advancement of material design and improvement of opto-electronic features, the simultaneous existence of multiple processes like carrier diffusion, photon recycling, and photon transport makes it often complex to differentiate them. In this study, we unravel the diverse yet dominant excitation energy transfer mode(s) in crystalline $MAPbBr_3$ micron-sized 1D rods and plates by localized (confocal) laser excitation coupled with spectrally-resolved wide-field fluorescence imaging. While rarely used, this technique can efficiently probe excitation migration beyond the diffraction limit and can be realized by simple modification of existing epifluorescence microscopy setups. We find that in rods of length below ~2 microns, carrier diffusion dominates amongst various energy transfer processes. However, the transient non-radiative defects severely inhibit the extent of carrier migration and also temporarily affect the radiative recombination dynamics of the photo-carriers. For $MAPbBr_3$ plates of several tens of micrometers, we find that the photoluminescence (PL) spectral characteristics remain unaltered at short distances ($< \sim 3\ \mu m$) while at a larger distance, the spectral profile is gradually red-shifted. This implies that carrier diffusion dominates over small distances, while photon recycling, *i.e.*, repeated re-absorption and re-emission of photons, propagates excitation energy transfer over extended length scales with assistance from wave-guided photon transport. Our findings can potentially be used for future studies on the characterization of energy transport mechanisms in semiconductor solids as well as for organic (molecular) self-assembled microstructures.

1. Introduction

Effective long-range exciton transport (migration) in molecular aggregates/ solids plays a crucial role in the application of (opto)electronic and photovoltaic devices [1, 2]. In natural photosynthetic system, the photo-generated excitons transport directionally in a sophisticated manner from the light-harvesting center to the reaction center [3], which is indeed a source of inspiration for research on artificial counterparts [4–6]. In case of self-assembled organic J- and H- molecular aggregates and polymers, the carriers can diffuse to a distance of few tens to hundreds of nm with effect of incoherent and coherent exciton migration or by a combination of both processes [7–9]. In inorganic semiconductor quantum dots (QDs) and nano-crystal (NCs) films, the diffusion distance has been reported to be of few tens of nm [10, 11], which notably depends on the individual crystal size and material compositions, and the density of energetic disorders [10–13]. Further, in CdSe-based laterally stacked self-assembled structure of nano-platelets, and micron-sized QD superlattice,

the energy can diffuse up to a few hundreds of nm [14, 15]. Therefore, a detailed and thorough understanding and analysis of energy diffusion are essential for efficient charge migration and collection, which can significantly enhance the device performance and can help to develop new exciton (photonic) devices.

The recent development of organic/inorganic metal halide perovskites (MHPs) have achieved a remarkable breakthrough in optoelectronic and photovoltaic applications [16–18], by virtue of its superior optical properties like high absorptivity and photoluminescence (PL) quantum yield [19], tunable bandgaps [20], controllable dimensionalities [21, 22], and cost-effective preparations [23]. Remarkably, it is well documented that the MHPs have long carrier diffusion length [24], owing to their long carrier lifetime and high photo-carrier diffusivity [25, 26]. Besides, the high absorption coefficient and the extensive overlap of absorption and emission spectra in MHPs lead to self-absorption of the high energy emanated photons followed by radiative re-emission [27, 28]. The iterative process of multiple such events results in recycling of the photon within the excited material over a larger distance in the crystal [29, 30]. Although photon recycling (PR) improves the open-circuit voltage of the solar cells [1], the self-absorption of photons is detrimental for light-emitting applications [31]. Furthermore, the optical waveguide of emanated photons owing to total internal reflection (TIR) in perovskites assists to retain a considerable fraction of emission from escaping the structures and guides over a longer distance [30, 32]. Therefore, it is essential to differentiate and control the pathways of long-range energy transport in perovskite crystals/films, which can be helpful for their application in devices.

In the last few years, it has been observed that the photo-generated carriers in various MHPs structures like micro-rods (MRs) and micro-discs (MDs) show long-range effective carrier communication up to few microns, which can lead to spatially-synchronous PL intermittency of entire bulk perovskite crystals [33–35]. Further, it has been reported recently that this communication, essential for spatially-correlated emissivity fluctuations between fused crystal (conjoined) grains, can be interrupted intermittently via effective yet fleeting energy barriers formed at the grain boundaries owing to charged defects formed therein [36]. Although the explicit nature and origin of transient defects are poorly understood, the presence of environmental factors like moisture, oxygen, and light significantly perturbs their formation and annihilation [37–39]. Therefore, to understand the dynamics of energy transport in the presence of metastable quenchers, it is crucial to use unconventional imaging methods to probe the extent of excitation energy migration in large (microns or beyond) crystals.

A wide range of techniques has been reported so far to measure the diffusion length, such as PL quenching [40], space-charge limited current [41], Hall coefficient measurements [24], and time-resolved microwave conductivity [42]. However, most of the methods necessitate the deposition of electrodes, which may not be practical for a few micron-sized structures. In recent times, remarkable progress has been made using microspectroscopic techniques. Exciton diffusion in solids with shorter propagation lengths has been extensively studied with ultrafast transient absorption microscopy [7, 43]. Although the measurements provide high temporal resolution in diffusion length [43], the length scale probed by this technique may be limited by the associated microscopy configuration as well as the scanning speed. On the other hand, there are alternate approaches to directly measure the exciton PL via local excitation and scan over the sample to collect the emission [30, 44]. However, these miss out the real-time simultaneous imaging of the entire sample, which is crucial to understand the impact of transient quenchers in long-range energy diffusion and the communication over the entire crystal. Due to the unavailability of a general method, the dynamics of distinct energy transport pathways in perovskites and how these get impeded with the presence of non-radiative quenchers, the defining characteristics of perovskites and other semiconductors, remain elusive.

In this work, owing to the relatively large size (much more than the diffraction limit) of MHP rods, discs, and plates, we used a simple yet rarely exploited technique of confocal (local) excitation followed by wide-field emission imaging [8, 9] to probe excitation energy migration in various perovskite micro-structures. Slight modifications in our existing wide-field fluorescence microscope allowed us to design a switchable imaging setup equipped with both wide-field (*WF*) and confocal (*CF*) excitations while being able to image the emission from the entire sample as well as collect spatially-resolved fluorescence spectra from various locations beyond the excitation spot. This method offers a unique opportunity to trigger the formation of charge carriers locally (within diffraction limit), and probe the subsequent radiative recombination locally as well as at different spatial regions owing to excitation energy transport processes. Here, using local excitation followed by collection of spectral emission as a function of distance from the excitation point, we illustrate the extent and nature of various long-range energy transport mechanism(s) in various $MAPbBr_3$ perovskite micro-structures. Further, we show that the formation of metastable non-radiative traps can severely hamper, albeit transiently, long-range energy transport in perovskite micro-rods.

2. Materials and methods

2.1. Syntheses and sample preparations

2.1.1. Chemicals

Methyl amine (CH_3NH_2, 33 wt% in ethanol, Spectrochem Pvt. Ltd), Hydrobromic acid (HBr, 47 wt% in

H_2O, Spectrochem Pvt. Ltd), Ethanol (99.9%, Changshu hongsheng fine chemicals Co. Ltd), Oleic acid (OA, >90%, Aldrich), n-Octylamine (99%, Aldrich), N,N-Dimethylformamide (DMF, Spectrochem. Pvt. Ltd), Toluene (>99.5%, merck life science Pvt. Ltd), Lead (II) bromide ($PbBr_2$, >99%, Lobachemie. Pvt. Ltd). All the chemicals were used as received without any further purification.

2.1.2. $MAPbBr_3$ micro-rods (MRs)

The syntheses, structural and optical characterizations of methylammonium bromide (MABr) and methylammonium lead bromide ($MAPbBr_3$) 1D rods are provided in earlier reports [33, 35]. In brief, the equimolar mixture of MABr and $PbBr_2$ were dissolved in 2 ml of DMF. Oleic acid (0.5 ml) and n-octylamine (30 μl) were added as capping groups to the solution mixture and were stirred for 5 min till the complete dissolution of precursors. Finally, 8 ml of toluene was added dropwise to the solution. The final solution was stirred for ~24 h at room temperature (~298 K) under ambient conditions for the growth of $MAPbBr_3$ 1D rods. The sample was then washed and centrifuged with toluene at 5000 rpm for 10 min and dried under vacuum for further measurements. For the microscopic measurements, MRs in toluene was spin-cast on a glass coverslip (Fisher Scientific, 25 × 25 #1) at 2000 rpm for 1 min.

2.1.3. $MAPbBr_3$ micro-discs (MDs)

The syntheses, structural and optical characterizations of $MAPbBr_3$ micro-discs are provided in earlier report [35]. In sort, 0.22 M of MABr and 0.2 M of $PbBr_2$ were dissolved in DMF. The amount of MABr was kept slightly excess (10%) than $PbBr_2$. The resultant precursor solution was spin-cast on a cover-glass at 2000 rpm for 1 min and annealed at 90 °C. It results in formation of $MAPbBr_3$ micro-discs (MDs) on the glass surface.

2.1.4. $MAPbBr_3$ micro-plates (MPs)

We synthesized the tens of micron-sized $MAPbBr_3$ plates with slight modification of earlier report [45]. An equimolar mixture of MABr and $PbBr_2$ were dissolved in DMF to prepare ~0.05 M precursor solution. 50 μl of precursor solution was directly dropped on top surface of a cover glass and was placed in a petri-dish. The petri-dish was kept in a beaker with toluene below the edge of the petri-dish and was sealed with porous aluminum foil. The nucleation and subsequent growth of $MAPbBr_3$ MPs will take place with the diffusion of anti-solvent toluene vapor into the precursor solution. After 24 h, micron-sized plates were left on the cover glass.

2.2. Microscopy setup

For spatio-temporarily and spectrally resolved photoluminescence (PL) measurements, we used a home-built epifluorescence microscopy setup; the details of optical arrangements can be found in the earlier report [46]. The sample was illuminated with a continuous-wave (CW) 488 nm DPSS laser (LBX-488, Oxxius) with an oil immersion objective lens (60X, 1.49 NA, Apo TIRF, Nikon). The laser power was measured after the objective lens with a power meter (Laserscheck, Coherent) and was adjusted with neutral density (ND) filters. The emanated fluorescence emission was collected back by the same objective lens, and was passed through appropriate dichroic (Di01-R488, Semrock) and 514 nm long-pass emission filters (Semrock). The PL was recorded with an air-cooled sCMOS camera (sCMOS ORCA-Flash4.0 V3, Hamamatsu) at 20 fps as 16-bit TIFF files. The schematics of the microscopy setup are shown in figure 1. We flattened the background of the recorded movie before further analyses. ImageJ (NIH) [47], Origin8, and MATLAB (R2016a) are used for the analyses of all imaging data. All the PL measurements were performed at room temperature (295 K) at relative humidity (RH) of ~50%.

For confocal excitation, we allowed the collimated expanded laser beam to pass through the back-focal plane (BFP) of the objective lens, which focuses the beam at a diffraction limited point (FWHM ~300 nm) on the sample plane, as shown in figure 1(a) [8, 9]. The fluorescence emission was collected from an area (diameter ~25 μm), which is imaged using an array detector (sCMOS camera). For spatially-resolved spectroscopy, we positioned the slit of the home-built spectrograph in the emission path such that it encompasses the excitation spot within the slit, and the spectrally dispersed (first order) image was detected by the same sCMOS detector [46]. With point excitation, a high carrier concentration is expected at the central illumination spot where the carriers are formed. However, when there is long-range carrier migration, a gradual decay of carrier density is expected beyond the excitation spot (figure 1(b)(ii)). This should result in PL emission from an extended area beyond the illumination zone. Further, the extent of energy diffusion can be evaluated from the comparison of cross-section of intensity line profiles of PL emission to that of the laser excitation (figure 1(b)(iii)).

2.3. Optimizations and control measurements

Prior to the confocal excitation (Ex_{CF}) PL imaging, it is essential to perform several control measurements to ensure the retention of excitation focus under different experimental circumstances. To verify the stability of excitation focus at different laser power densities and integration time, we collected the back-reflected laser from a cleaned blank coverslip (figures 2(a), (b)). From the extracted intensity profiles along the horizontal and vertical dashed lines, as shown in figure 2(a)(i), (ii), we observed a nominal (~3%) change in excitation profile (8–10 nm) at high power denisity as compared

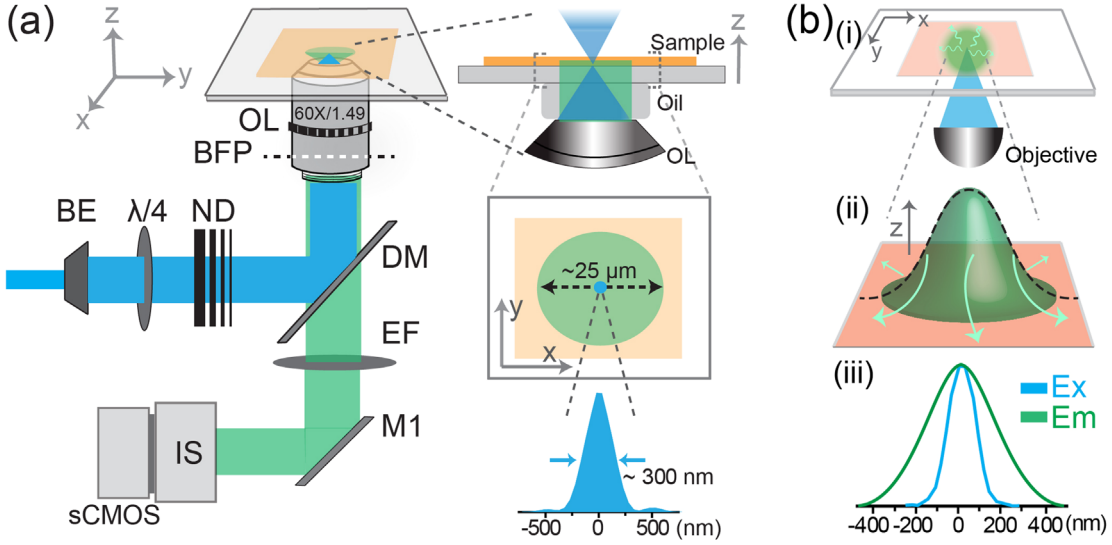

Figure 1. (a) Schematic representation of confocal excitation microscopy setup for spatio-temporarily and spectrally resolved photoluminescence (PL) measurements. Parallel excitation beam is passed through BFP of objective lens. It focuses the excitation beam at a diffraction limited spot on sample plane of FWHM ~300 nm. The PL emission is collected over an area of diameter ~25 μm. (b) (i) Schematic illustration of energy diffusion away from the illumination spot with confocal excitation, (ii) charge carrier density profiles of the photo-generated carriers, (iii) cross-sectional line profiles along the dashed line of excitation (blue) and emission (green). (Abbreviations: BE-Beam Expander; $\lambda/4$-quarter wave-plate; ND-Neutral Density filter; DM-Dichroic Mirror; BFP- Back-Focal Plane; OL- Objective Lens; EF-Emission Filter; M1-highly reflective mirror; IS-Imaging Spectrograph).

to low power density. We note that the change in integration time did not artificially broaden the reflected laser beam profile (figure 2(b)(i), (ii)).

The coexistence of both excitation as well as emission focus in the same focal plane is crucial for Ex_{CF} PL imaging. For that, we excite next to a $MAPbBr_3$ perovskite MR (MR-1) at high excitation power density (~1 $kWcm^{-2}$) so that it will have enough scattered light (near the illumination spot), which can excite the MR and results in detectable PL emission. Figure 2c(i) shows the PL image of MR-1 along with the laser excitation spot, which reveals the simultaneous focus of both excitation as well as PL emission. The wide-field excitation (Ex_{WF}) PL image of MR-1 is in the inset. Further, to eliminate the possibility of direct excitation of sample away from the excitation spot with the out coming scattered light, we imaged MR-1 at different excitation power densities (figure 2(c)). In figure 2(c)(iv), we can observe that MR-1 did not have a detectable PL emission at several fold of low power density (~10 Wcm^{-2}). So, we performed all our Ex_{CF} imaging at ~20 Wcm^{-2}.

Moreover, to eliminate the possibility of additional scattering of illumination light by the thickness of the sample, which may artificially broaden the excitation beam profile, we imaged the back-reflected laser from a microscopic cover-glass with ~100 nm diameter non-fluorescent polystyrene (PS) film (figure 2(d)). The extracted line profiles along both x-and y-directions have almost equivalent FWHMs, as that obtained from a blank cover glass. This illustrates that the sample thickness does not artificially alter the excitation beam shape/size. Further, we collected the PL of Rhodamine-6G (Rh-6G) film on a glass coverslip. To get the excitation profile, we selectively used a band-pass filter (420–500 nm) in the emission path, which allows only the excitation light (figure 2(e)(i)). For the fluorescence emission, a 514 nm long-pass (514 LP) filter was used (figure 2(e)(ii)). As Rh-6G molecules are not expected to have long range energy transfer, the identical line profiles of PL excitation and emission in figure 2(e)(iii) further eliminate the possibility of scattering of excitation light even from a fluorescent sample and reveal the localization of excitation energy.

Finally, to eliminate the possibility of (wave)guided propagation of excitation light in perovskite crystals as an origin of extended PL emission, we evaluated the laser beam profiles for the excitation point outside and on the MR. For simultaneous imaging of excitation spot (back reflection of laser) and PL from MR, we removed the emission filter and increased the excitation power density to 1 kW cm^{-2}, so that there is enough scattered light (near the illumination spot) which is able to excite the nearby MR and some PL emission from it could be detected (figure 2(f)(i)). The PL images were collected through two different energetic emission filters to separate the excitation and emission. Figure 2(f)(ii) shows the PL image of the excitation point only when the MR-2 is excited, whereas figure 2(f)(iii) shows the corresponding PL emission of MR-2, which was clearly elongated along the long axis of the rod. The intensity profiles along the dashed lines (figure 2(f)(iv)) reveal no significant change in the excitation beam profile even after placing the excitation point on the MR. A very similar behavior was observed for the excitation beam profile when the centre of an micro-disc was illuminated

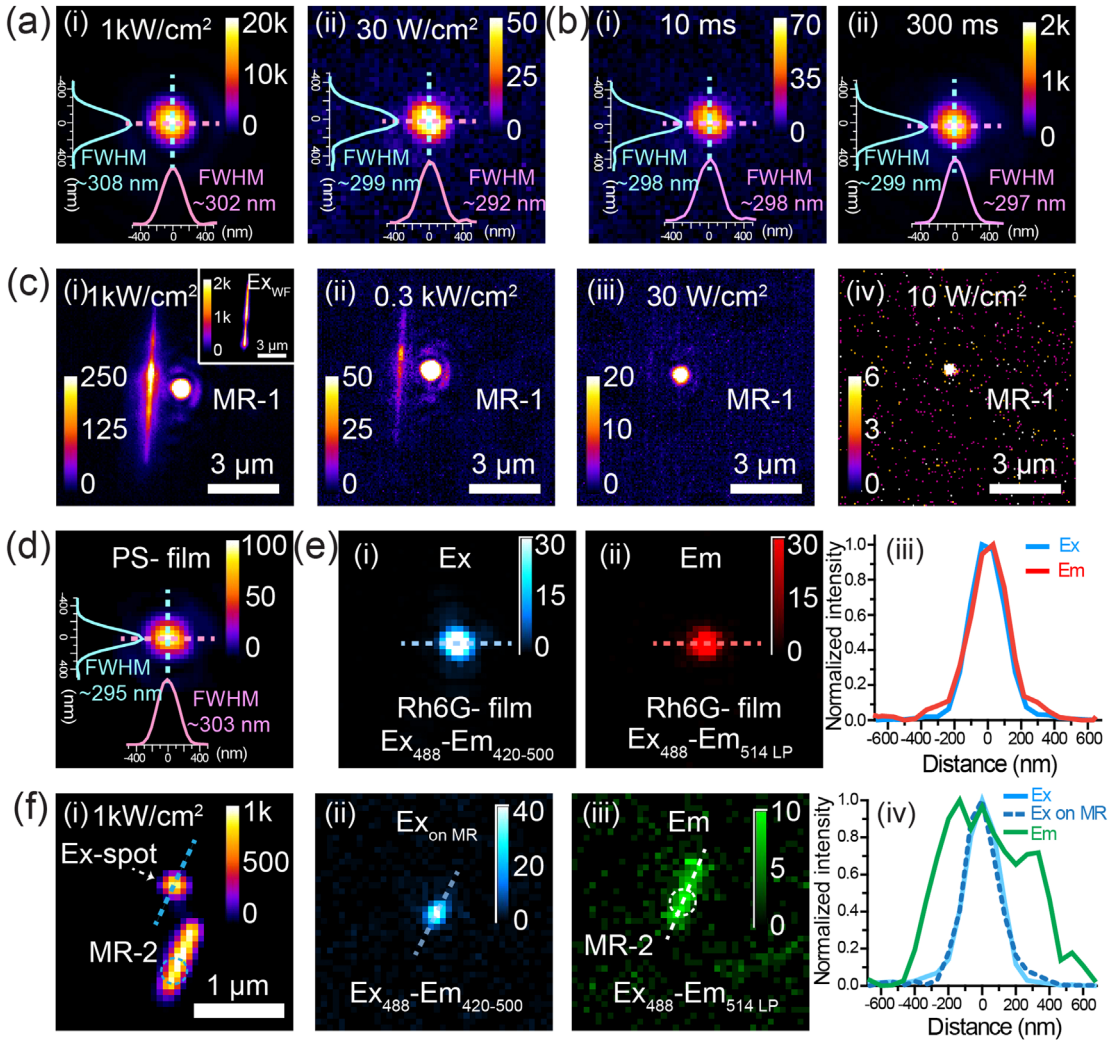

Figure 2. Control measurements for confocal-excitation wide-field imaging. PL intensity image of excitation focus back-reflected from a blank cover-glass along with line-profiles along dashed lines in x- and y-directions for different (a) excitation power densities and (b) integration times. (c) PL intensity images of a micro-rod (MR-1) with excitation next to the rod at different excitation power densities. The scattered light excited PL image in (c (i)) reveals the simultaneous focus of both excitation and emission. The wide-field image (Ex_{WF}) of MR-1 is in (c (i)) inset. (d) PL image of excitation focus back-reflected from cover-glass with ~100 nm thick non-fluorescent polystyrene (PS) film. (e) PL intensity image of Rhodamine-6G (Rh-6G) film of (i) only laser excitation without PL of Rh6-G, (ii) only PL of Rh6-G, and (iii) corresponding line-profiles along dashed lines, excitation (blue), and emission (red). (f) (i) Single camera average PL intensity image of MR-2 along with excitation spot outside the MR, collected without emission filter at a power density of 1kWcm^{-2}, average PL intensity image of (ii) excitation spot on MR without PL (iii) only PL of MR-2, (iv) their corresponding line-profiles along dashed lines, excitation spot outside MR (solid blue line), on the MR (dashed deep blue line) and PL of MR-2 (solid green line). All PL measurements were performed at excitation power density of 20 Wcm^{-2}, unless it is mentioned otherwise.

(figure S1 (available online at stacks.iop.org/MAF/10/044013/mmedia)). These measurements eliminate the possibility of waveguided transmission of the unabsorbed excitation light in $MAPbBr_3$ micro-crystals. That we could detect significant PL emission from an extended area over the long axis of the crystals (see figure 2(f)(iv) and results) beyond the excitation zone indicates radiative recombination after long-range excitation energy migration.

3. Results and discussions

To realize and explore the energy transport in various micron-sized structures of methyl ammonium lead bromide ($MAPbBr_3$) perovskite such as disc (MD), plates (MP), and rods (MRs), we imaged them with both wide-field and confocal illumination. The wide-field excitation average PL intensity image in figure 3(a)(i) shows a typical few micron-sized circular $MAPbBr_3$ micro-disc (MD-1). To probe the energy migration in the perovskite disc, we selectively excited at the center and collected the PL emission from the entire crystal. The average PL intensity image of MD-1 with local excitation spot is shown in figure 3(b)(i). Interestingly, we observed PL from an extensively broad area than the illumination spot (blue filled circle), which shows that the photo-excitation energy diffuses away from the illumination point. A careful inspection of the extracted line profiles of PL emission

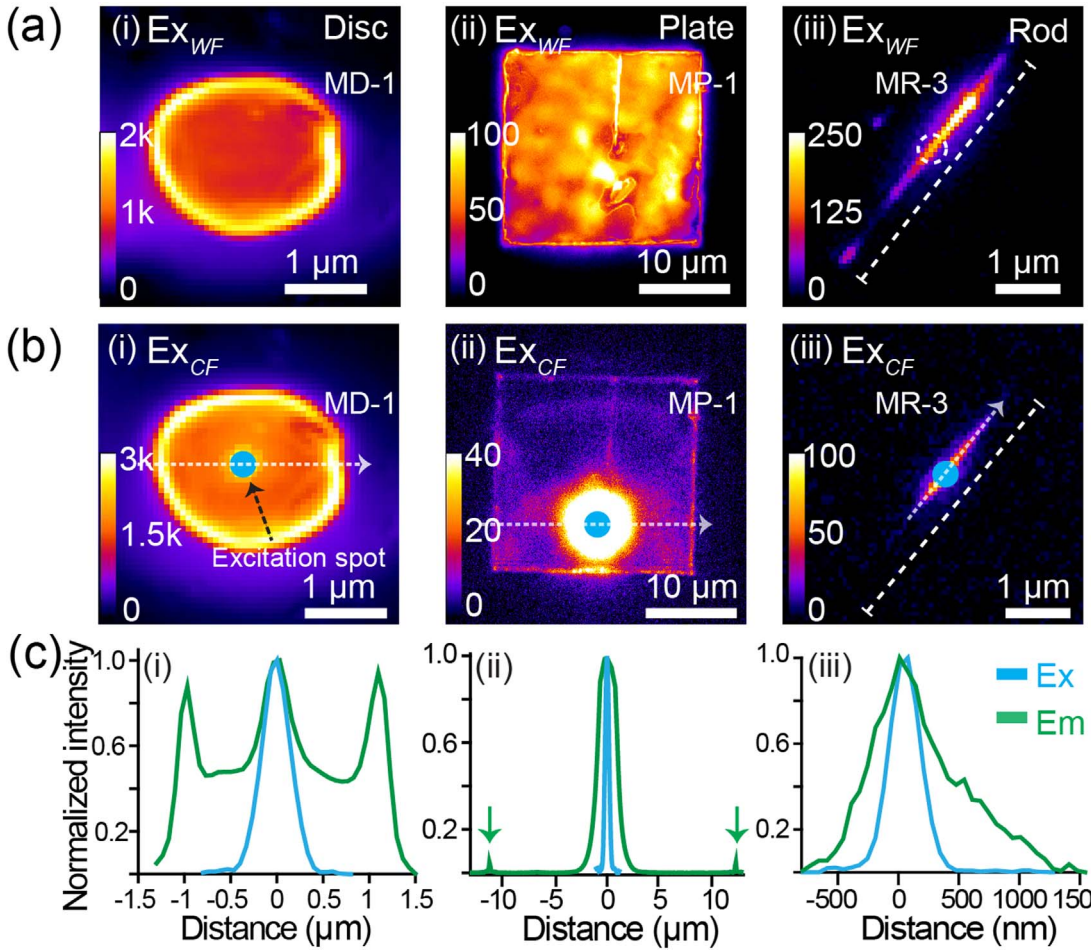

Figure 3. Average PL intensity images of micron-sized $MAPbBr_3$ disc , plate, and rod with a(i-iii) Wide-field excitation (Ex_{WF}), and b (i-iii) confocal excitation (Ex_{CF}), respectively. The excitation positions in Ex_{CF} are marked with blue filled circles. The contrast in b(ii) is adjusted to show the crystal edges, which makes to look the excitation spot bigger. The length of rod is shown with white dashed line. The intensity line profiles along the dashed arrows of emission (green) and excitation (blue) for $MAPbBr_3$ disc, plate, and rod are in c(i–iii), respectively.

and laser excitation along the dashed arrow (figure 3(c)(i)) reveals a relatively higher PL emission at the illumination point, followed by a gradual decrease in PL intensity away from the excitation spot. However, significantly enhanced emission was observed at the crystal edges, which illustrates the diffusion of photo-excitation energy up to few microns away from the illumination spot over the entire disc. Further, significant emissivity at the crystal edges reveals that the dimension of individual crystals constrain the extent of energy migration within the perovskite disc.

To explore the energy transfer in larger $MAPbBr_3$ objects, we imaged a plate of few tens of micron-size (MP-1) with wide-field excitation (figure 3(a)(ii)). Here too, with Ex_{CF}, we observed extended emission from the entire plate (figure 3(b)(ii)). Here, the contrast has been adjusted to show the emission from the edges, which make the excitation spot seem much bigger in size compared to that for the MD. Next, to evaluate energy migration, we extracted the intensity profiles along the dashed arrow and plotted in figure 3(c)(ii). This reveals that the dominant emission is near the excitation point, and intensity gradually decreases on moving away from that spot, however, there reduction of emission intensity is far less abrupt as compared to the excitation light. Remarkably, a weak enhancement in emission was observed even at the edges of MP-1, which can be seen from the line profiles (figure 3(c)(ii)). This illustrates the effective excitation energy migration up to ~10 μm distance from the illumination point in $MAPbBr_3$ microplates.

The MPs and MDs are single crystalline and polycrystalline in nature, respectively [35, 45]. The nature of crystallinity can severely affect photo-carrier lifetime, and thus the corresponding diffusion distances. In addition, the dimension of crystal and the extent of stokes shift (spectral overlap of absorption/emission) can modulate the relative contributions of energy transfer pathways over the migration distance. Therefore, it is reasonable to speculate that the aforementioned structural and optico-electronic differences are likely to be responsible for the PL emission behaviors over the MPs and MDs.

Further, we analyze the energy migration in a few micron-sized one-dimensional (1D) $MAPbBr_3$ micro-rod (MR-3), where the transport of carriers or energy is primarily confined along longitudinal axis of the crystal (figure 3(a)(iii)). Interestingly, when we irradiated locally at the middle of MR-3 (dashed circle in figure 3(a)(iii)), we observed asymmetric energy transport on both sides of the excitation point(figure 3(b)(iii)). The corresponding line profiles (figure 3(c)(iii)) along the long axis further reveals that on one side, energy diffusion is limited to few hundreds of nanometers, while in other direction, excitation can migrate to ~1 μm. This reveals that the migration lengths are not limited by the dimensions of MR, in contrast to discs and plates of the $MAPbBr_3$ where the size of the crystal primarily determines the diffusion length. It has been reported that the presence of highly efficient quenchers (defects or traps) in MHPs is highly detrimental, and can severely affect the energy migration by funneling the carriers through non-radiative (NR) channels [25, 48]. We note that even with uniform wide-field illumination of entire MR-3, attenuated emission is observed at the (lower) side of the rod (figure 3(a)(iii)), which unambiguously points to the presence of highly efficient NR defects on one side of the excitation spot. We further note that MRs did not show any enhanced emission at the rod ends, contrary to that observed in MDs and MPs, signifying a lack of waveguided photon transmission over long distances.

To further explore such non-uniformity in terms of position and efficiency of NR defects, as well as their effect on energy propagation in MRs, we selected 25 MRs with length of at least ~2 μm, and excited (locally) near their centre. We find both symmetric as well as asymmetric energy transport on both sides of illumination point, as exemplified in figures 4(a-d)using two representative MRs (MR-4/-5) following wide-field and confocal illumination. As the emission of MRs have non-Gaussian intensity profiles, we refrain from using the conventional deconvolution analyses to calculate the diffusion distances [49]. Instead, we first compared PL emission of Rh-6G film with Ex_{CF}, where the excitation energy remains confined within the illumination spot with respect to the excitation profile (figure 2(e)). This value turns out to be ~20% of the maximum PL intensity, which we select as the accuracy limit of our measurement, and is also well above the background intensity levels (figure S2). Therefore, we evaluated the energy migration distances on both sides of each MR from the central position, at 20% of the peak amplitude(figures 4(c), (d)). The extracted migration lengths (L_1, L_2) of individual MRs (figure 4(e)) shows a mean of ~600 nm with some variation in the migration lengths amongst the MRs. As seen from figures 4(c), (d), MR-4 has symmetric and slower intensity fall, whereas, MR-5 has asymmetric and steeper intensity fall on one side. The asymmetric, steeper intensity fall for MR-5 can be attributed to the presence of highly efficient quencher(s) either one side, or distinct quenchers on both sidenear the vicinity of the illumination point. Further, to evaluate the population of MRs with symmetric and asymmetric energy migration, we plotted the distribution of ratio of difference in migration lengths (figure 4(f)) on both sides to maximum migration length ($|L_1 - L_2|/L$, where L is larger value between L_1 and L_2). This analyses demonstrates the heterogeneity in terms of spatial locations as well as quenching efficiency of NR defects amongst MRs.

Interestingly, these NR traps or quenchers are often metastable, i.e., are transiently formed and affect the radiative recombination of photo-carriers, which results in multi-state PL intermittency of entire crystal over a timescale of few tens of milliseconds to seconds [33, 35] depending on the crystal being investigated. The PL fluctuation occurs over a base emission intensity likely due to the faster local radiative recombination dynamics before carriers undergo long-range diffusion,. Over the last few years, effective long-range carrier communication amongst photo-generated carriers up to few microns has been observed in various MHP crystals, such as rods and discs [33–35]. The formation/annihilation of highly efficient metastable NR traps (quenchers) with the effect of photo-irradiation and interactions with environmental constituents transiently funnel the carriers in non-radiative pathways [33], which results in spatially extended concerted PL intermittency of the entire crystal. Interestingly, inter-crystal communication has also been observed between conjoint crystals, which is often interrupted transiently [36]. However, such intriguing phenomena are reported with wide-field illumination, where the photo-carriers are generated over the entire crystal. Therefore, to investigate the formation of transient NR traps and their effects on carrier diffusion and subsequent PL recombination, we selectively excited a rod (MR-6, figure 5(a)) at one end and monitored the PL recombination dynamics over the entire rod and intriguingly, we observed PL fluctuations of the entire micro-rod! The observed PL instability of MRs is inherent to the crystal itself, and does not result from laser intensity fluctuations (figure S3). To probe the spatial dependence of PL fluctuations, we extracted the PL intensity traces from three distinct nano-domains of the MR-6. The normalized PL intensity trajectories of these locations (designated as *I*, *II*, *III* in figure 5(a)) and the average intensity trace of entire MR-6 are plotted in figure 5(b). The multiple intensity levels traces are nearly indistinguishable and temporally superimposable. For better visualization, the time-lapse sequential PL snapshots of MR-6 at distinct intensity levels (marked in figure 5(b)) are shown in figure 5(c), which clearly indicates the simultaneous enhancement and reduction in intensity of the entire MR-6. However, irrespective of the PL intensity level, a higher emission is always observed at the illumination point, and the intensity gradually decreases with distance away from the excitation spot. This reveals

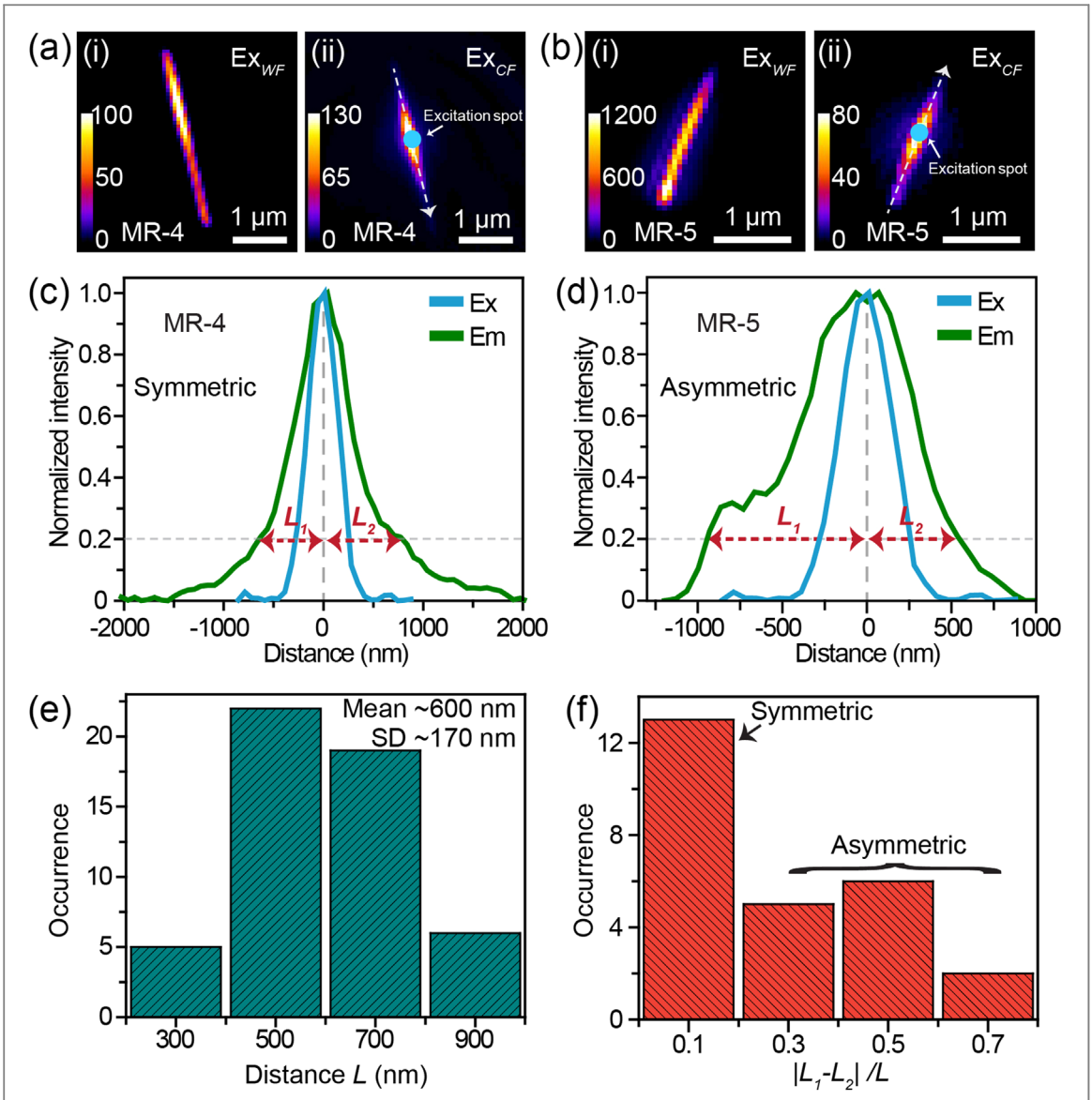

Figure 4. Average PL intensity images of MR-4/-5 with wide-field (Ex_{WF}) and confocal (Ex_{CF}) excitation in (a) and (b), and the corresponding intensity line profiles with Ex_{CF} along the dashed arrows of emission (green) and excitation (blue) in (c) and (d), respectively. The excitation positions are marked with blue filled circles. L_1 and L_2 are the energy migration lengths in MRs from central position at 20% of the peak amplitude. (e) Distribution of energy migration lengths of MRs, with mean ~600 nm, and standard deviation (SD) ~170 nm. (f) Distribution of [$|L_1 - L_2|/L$] of MRs, where L is larger value between L_1 and L_2, showing the populations of MRs with symmetric and asymmetric energy migration on the two sides of the excitation spot.

that the energy after photo-excitation undergoes effective diffusion over the entire MR. However, the highly efficient yet metastable NR traps effectively channel a significant proportion of energy in non-radiative pathways, thereby resulting in spatio-temporarily correlated PL intermittency of the entire MR.

The exciton binding energy of $MAPbBr_3$ perovskite bulk single crystal has been reported to be ~40 meV [50]. Therefore, the existence of both excitons and free carriers at room temperature (~295 K) is anticipated. The high diffusivity and long lifetime of the photo-generated carriers assist the long-range exciton/carrier diffusion [24–26] accompanied by radiative recombination. However, the high absorptivity of the perovskite material leads to self-reabsorption of higher-energy emitted photons, followed by re-emission [28]. Such recycling of the emitted photon by an iterative process of multiple re-absorption and re-emission (photon recycling) facilitates migration of energy far away from the illumination spot [30]. However, with the migration distance, the spectral envelope of the emitted photons can get skewed towards the lower energy [30]. Besides, total internal reflection in perovskites with high refractive index allows directional propagation of emitted photons, which escape from the edges [32] leading to intense PL at the crystal edges.

Therefore, to distinguish the different energy propagation pathways like carrier diffusion, photon-recycling, and optical waveguiding, we performed spatially and energetically resolved PL imaging by acquisition of PL emission through a higher and lower energy detection channels, i.e., a green (492–536 nm) and a

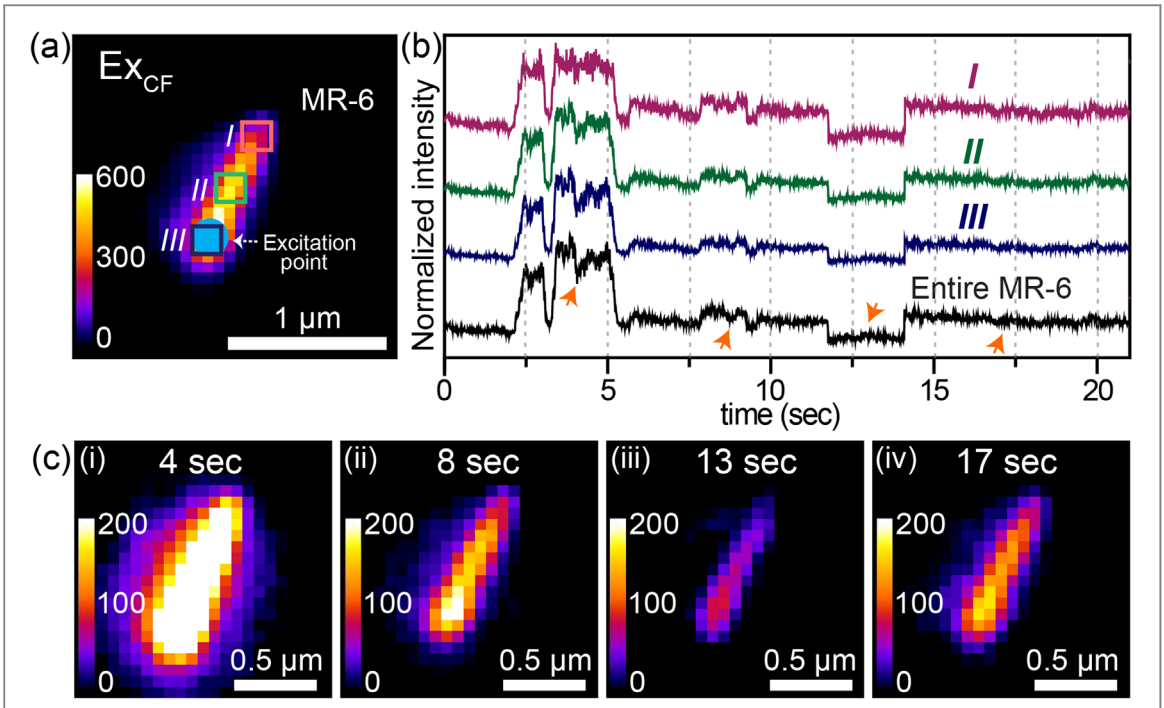

Figure 5. (a)PL intensity image of a micro-rod (MR-6) with confocal excitation (Ex_{CF}). The excitation spot is marked with blue filled circle. (b) Normalized PL intensity trajectories of three different spatial nano-domains (I-III), as shown in (a), along with the normalized intensity trajectory of entire MR-6, which shows indistinguishable PL intensity fluctuations. (c) The time-lapse sequential PL snapshots of MR-6 at different intensity levels, marked with arrow heads in (b), show simultaneous enhancement and reduction of PL intensity of entire MR-6.

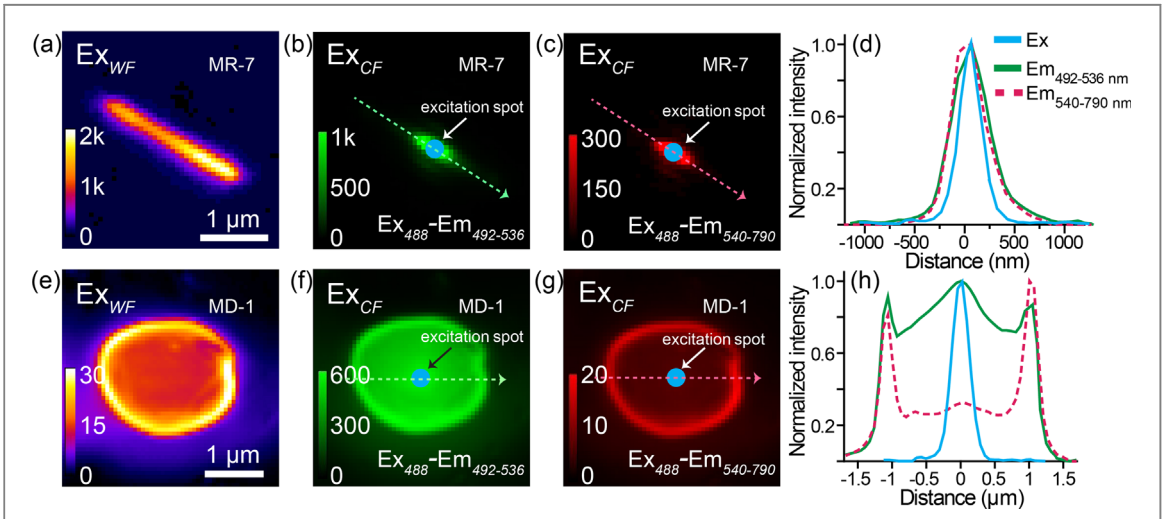

Figure 6. Wide-field excitation (Ex_{WF}) average PL intensity images of micron-sized $MAPbBr_3$ rod MR-7 in (a) and disc MD-1 in (e). Average PL intensity images of MR-7 and MD-1 in two energetic channels of 492–536 nm and 540–790 nm with confocal excitation (Ex_{CF}) in (b), (c) and (f), (g), respectively. The excitation positions are marked with blue filled circles. Normalized intensity profiles along the dashed arrows of excitation (solid blue), emission through 492–536 nm filter (solid green) and through 540–790 nm filter (dashed red) for MR-7 and MD-1 in (d) and (h), respectively.

red (540–790 nm) emission filter. The wide-field PL images of a rod (MR-7) and a disc (MD-1) are shown in figures 6(a), (e). Interestingly, with local excitation in MR-7, we observed analogous spatial distribution of PL in both green and red channels (figures 6(b), (c)), which can be seen in the normalized intensity line profiles (figure 6(d)). However, with local excitation in MD-1, we observe relatively homogeneous emission through the green channel over the entire crystal (figure 6(f). In stark contrast, low energy (red) emission is mostly located at the crystal edges (figures 6(g)). The intensity line profile in figure 6(h) reveals that high energy emission in MD primarily owes to the recombination of diffused photo-carriers, however, a proportion of the emitted photons get iteratively recycled over the migration distance. The re-emitted low energy photons are wave-guided, and eventually escapes from the crystal edges.

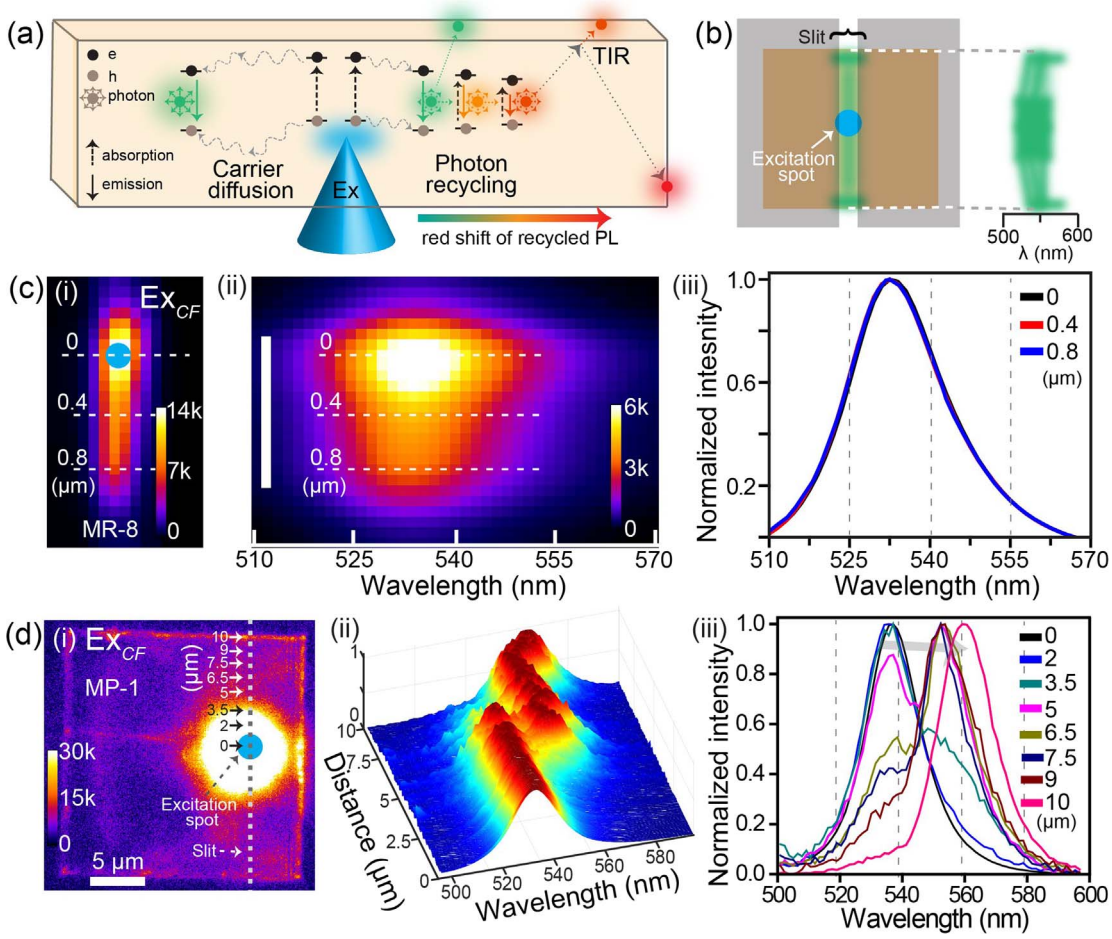

Figure 7. Schematic illustration of long-range energy transfers in micron-sized MHP crystal via carrier diffusion, photon recycling, and wave-guided transport of emitted photons by total internal reflection (TIR). (b) Schematics for spatially resolved spectroscopy of MHP micro-crystal with confocal excitation (Ex_{CF}). (c) PL intensity image of micro-rod (MR-8) with Ex_{CF} is in (i), and corresponding spectral image in (ii). Excitation spot is marked with blue filled circle. (iii) Normalized PL spectra of three distinct nano-domains 0, 0.4, and 0.8 μm away from excitation spot. (d) (i) PL intensity image of micro-plate (MP-1) with Ex_{CF}. The contrast of the image is adjusted to show the edges makes to look the illumination spot bigger. The slit position is marked with a dashed line. (ii) Normalized emission spectral profile of MP-1 from Ex_{CF} spot to crystal edge showing the gradual low energy spectral shift on moving away from Ex_{CF} spot. (iii) Normalized PL spectra of distinct nano-domains, marked in d(i).

To corroborate these processes (schematically described in figure 7(a)) following local excitation, we explored the emission spectral behavior with the propagation distance using spatially-resolved fluorescence spectroscopy (figures 7(b)). We excited a perovskite rod (MR-8) at one end and collected the spectra along the long axis. The PL intensity image and the corresponding spectral image of the rod are shown in figure 7(c)(i), (ii), which reveal a gradual decrease in PL intensity with increasing distance from the illumination spot. Here, we did not observe any intense emission at the tips of MR in Ex_{WF} as well as Ex_{CF} micro-spectroscopy measurements (figures 3(a)(iii), 6 and 7(c)), which eliminates the feasibility of wave-guided transmission of photons in micro-rods [32, 51]. Further, we extracted the spectral profiles from three distinct spatial nano-domains, at 0, 0.4, and 0.8 μm away from the Ex_{CF} spot, and the corresponding normalized PL spectra (figure 7(c)(iii)). Interestingly, we did not observe any noticeable variation in emission energy as well as in the spectral envelope, which suggests the nominal contribution of photon recycling (PR) in long-range energy transfer. Similar spectral characteristics have been recently observed in perovskite micro-wires, and have been primarily attributed to the active participation of carrier diffusion [52]. Therefore, we infer that charge carrier diffusion is the dominant energy transport pathway in the $MAPbBr_3$ perovskite micro-rods for long-range carrier communications.

Next, we investigated the long-range energy transport mechanisms in $MAPbBr_3$ perovskite microplates. The PL intensity image of a plate (MP-1) with Ex_{CF} is shown in figure 7(d)(i), along with a vertical line from which emission spectra was collected. To obtain spectral information as a function of distance from excitation spot, we plotted the normalized dispersed emissionspectral image up to the crystal edge (figure 7(d)(ii)), which reveals a clear shift in emission energy on moving away from the illumination center. Further, we extracted the emission spectra from eight distinct nano-domains (marked in figure 7(d)(i))

located successively between the excitation spot and the crystal edge (figure 7(d)(iii)). Suprisingly, beyond ∼3 μm from the irradiation point, a new shoulder appeared at lower energy part of the spectral envelope. For the subsequent nano-domains, this new peak at ∼550 nm becomes dominant with concomitant attenuation of the initial higher energy (∼535 nm) peak. Intriguingly, at the crystal edges, ∼10 μm from the illumination spot, we find a further red-shifted relatively intense emission peak (at ∼560 nm). We have observed similar spectral behavior in other MPs as well (figure S4). However, the origin of the unusual red shift beyond acertain distance (∼10 μm) from the illumination point still remains unclear, and other processes such as exciton-photon coupling (polariton) or some other optical phenomenonmay be responsible for such an observation .

With the local illumination of MP, the photo-generated charge carriers diffuse away from the excitation regime. The observed minimal red-shift along with higher PL intensity emission at a shorter distance ($<$ ∼3 μm) illustrates that a substantial fraction of diffused photo-carriers recombine locally and result in band-to-band recombination-based PL emission. The observed gradual modulation in spectral profile with the increase in spatial separation of Ex_{CF} spot and emission point reflects re-absorption of primary photons (i.e., photons produced by the direct photo-excitation) at higher spectral energy, and enhanced PL contribution at longer wavelengths. Beyond ∼3.5 μm from the excitation point, repeated PR results in emergence of a shoulder owing to re-emission, which eventually dominates over the higher energy peak. We note that a similar spectral behavior has been recently reported for 1D $CsPbBr_3$ single crystal [30], ascribed to iterative PL self-re-absorption and re-emission of emanated photons (or PR). However, our findings are in contrast to an earlier report on $MAPbBr_3$ crystals [53], where self-re-absorption based spectral filtering modulate the PL emission spectra over long distances. Nonetheless, the photons of lower energy which emanate after repeated PR, are waveguided across the crystal and eventually escape at the boundaries resulting in slightly intense emission at the edges.

Our Ex_{CF} micro-spectroscopy results on MPs reveal that for shorter distances (up to ∼3 μm from the excitation point), mostly carrier diffusion process dominates over the other energy transport processes. Whereas, for longer distances ($>$3 μm), PR is activeky involed in energy migration, as evidenced from the observed spectral characteristics (figure 7(d)(iii)). Therefore, we speculate that PR plays an extensive role in the long-range energy migration in $MAPbBr_3$micro-plates, however, the involvement of carrier diffusion and guided transmission of the photons cannot be neglected.

Despite this illustrated imaging method is able to distinguish the distinct energy transport pathways in different perovskite crystals, it is still unable to quantitatively provide the relative contributions of each individual process for long-range excitation energy migration. In earlier reports, the time-resolved PL decay over distal spatial locations was fitted with distinct simulated models, which account for the different energy transport pathways [30, 52]. The knowledge of excited carrier population at the illumination zone, carrier mobility, PL decay kinetics, and the evaluation of extinction coefficients where the absorption-emission spectra overlap, will be helpful to estimate relative contributions from distinct energy transport pathways.

4. Summary and outlook

To summarize, we have investigated the long-range energy propagation in various $MAPbBr_3$ structures using confocal excitation wide-field micro-spectroscopy measurements. Our Ex_{WF} and Ex_{CF} measurements and analyses on 1D few micron-sized perovskite rods reveal that the diffusion of photo-excited carriers mostly dominates the energy transport mechanisms. The formation of non-radiative energetic defects significantly impact the diffusion distance, as well as transiently hampers the long-range communication of the diffused photo-carriers in the micro-rods. Further, from spectral measurements and analyses on microplates, we surmise that the carrier diffusion primarily facilitates the short-range energy propagation ($<$∼3 μm). Over longer distance, the photon-recycling significantly expedites the long-range energy migration with assistance of guided transmission of photon in methyl ammonium lead bromide micro-plates.

The illustrated (spectral) imaging method with confocal excitation will be useful to observe and distinguish the distinct photo-induced charge-carrier and photon transport mechanisms in various perovskite/semiconductor micro-structures with diverse material compositions, as well as in homo-/hetero-structured (organic) molecular aggregates. Further, it will be beneficial to analyze the origin and nature of energetic defects in semiconductors, self-annealing of defects in material owing to ionic migrations, and the concomitant corollaries on distinct energy migration pathways. We therefore feel that this work will be valuable as a tool to analyze the defects and characterize the energy transfer processes in micro-structured perovskites and molecular aggregates, which can undoubtedly be helpful for photo-voltaic and light emitting applications.

Acknowledgments

A C acknowledges SERB (DST, Govt. of India) grant no. EMR/2017/004878 to carry out this work. The authors acknowledge IIT Bombay for usage of central facility equipment. A C acknowledges the MNRE (Govt. of India) funded National Center for

Photovoltaic Research and Education (NCPRE) at IIT Bombay for partial financial support. T.B. thanks CSIR (09/087(0914)/2017-EMR-l) (India) for PhD fellowships. NP thanks IIT Bombay for institute post-doctoral fellowship, and RM thanks PMRF aided PhD research fellowships.

Data availability statement

The data that support the findings of this study are available upon reasonable request from the authors.

Conflict of interest

The authors declare no conflict of interests.

ORCID iDs

Tejmani Behera https://orcid.org/0000-0003-2995-9293
Nithin Pathoor https://orcid.org/0000-0001-5252-3979
Rajat Mukherjee https://orcid.org/0000-0001-5795-951X
Arindam Chowdhury https://orcid.org/0000-0001-8178-1061

References

[1] Lee S, Choi K, Min C H, Woo M Y and Noh J H 2020 Photon recycling in halide perovskite solar cells for higher efficiencies *MRS Bull.* **45** 439–48
[2] Menke S M, Luhman W A and Holmes R J 2013 Tailored exciton diffusion in organic photovoltaic cells for enhanced power conversion efficiency *Nat. Mater.* **12** 152–7
[3] Scholes G D, Fleming G R, Olaya-Castro A and Van Grondelle R 2011 Lessons from nature about solar light harvesting *Nat. Chem.* **3** 763–74
[4] Blankenship R E *et al* 2011 Comparing photosynthetic and photovoltaic efficiencies and recognizing the potential for improvement *Science* **332** 805–9
[5] Fleming G R, Schlau-Cohen G S, Amarnath K and Zaks J 2012 Design principles of photosynthetic light-harvesting *Faraday Discuss.* **155** 27–41
[6] Brixner T, Hildner R, Köhler J, Lambert C and Würthner F 2017 Exciton transport in molecular aggregates—from natural antennas to synthetic chromophore systems *Adv. Energy Mater.* **7** 1–33
[7] Wan Y, Stradomska A, Knoester J and Huang L 2017 Direct imaging of exciton transport in tubular porphyrin aggregates by ultrafast microscopy *J. Am. Chem. Soc.* **139** 7287–93
[8] Clark K A, Krueger E L and Vanden Bout D A 2014 Direct measurement of energy migration in supramolecular carbocyanine dye nanotubes *J. Phys. Chem. Lett.* **5** 2274–82
[9] Haedler A T, Kreger K, Issac A, Wittmann B, Kivala M, Hammer N, Köhler J, Schmidt H W and Hildner R 2015 Long-range energy transport in single supramolecular nanofibres at room temperature *Nature* **523** 196–9
[10] Lee E M Y and Tisdale W A 2015 Determination of exciton diffusion length by transient photoluminescence quenching and its application to quantum dot films *J. Phys. Chem.* C **119** 9005–15
[11] Akselrod G M, Prins F, Poulikakos L V, Lee E M Y, Weidman M C, Mork A J, Willard A P, Bulović V and Tisdale W A 2014 Subdiffusive exciton transport in quantum dot solids *Nano Lett.* **14** 3556–62
[12] Kholmicheva N, Moroz P, Bastola E, Razgoniaeva N, Bocanegra J, Shaughnessy M, Porach Z, Khon D and Zamkov M 2015 Mapping the exciton diffusion in semiconductor nanocrystal solids *ACS Nano* **9** 2926–37
[13] Kholmicheva N, Moroz P, Eckard H, Jensen G and Zamkov M 2017 Energy transfer in quantum dot solids *ACS Energy Lett.* **2** 154–60
[14] Liu J, Guillemeney L, Abécassis B and Coolen L 2020 Long range energy transfer in self-assembled stacks of semiconducting nanoplatelets *Nano Lett.* **20** 3465–70
[15] Yoon S J, Guo Z, Dos Santos Claro P C, Shevchenko E V and Huang L 2016 Direct imaging of long-range exciton transport in quantum dot superlattices by ultrafast microscopy *ACS Nano* **10** 7208–15
[16] Tsai H *et al* 2016 High-efficiency two-dimensional ruddlesden-popper perovskite solar cells *Nature* **536** 312–7
[17] Xiang W and Tress W 2019 Review on recent progress of all-inorganic metal halide perovskites and solar cells *Adv. Mater.* **31** 1902851
[18] Cho H *et al* 2015 Overcoming the electroluminescence efficiency limitations of perovskite light-emitting diodes *Science* **350** 1222–5
[19] Stranks S D and Snaith H J 2015 Metal-halide perovskites for photovoltaic and light-emitting devices *Nat. Nanotechnol.* **10** 391–402
[20] Xing G, Mathews N, Lim S S, Yantara N, Liu X, Sabba D, Grätzel M, Mhaisalkar S and Sum T C 2014 Low-temperature solution-processed wavelength-tunable perovskites for lasing *Nat. Mater.* **13** 476–80
[21] Ahmed G H *et al* 2017 Pyridine-induced dimensionality change in hybrid perovskite nanocrystals *Chem. Mater.* **29** 4393–400
[22] Yin J, Maity P, De Bastiani M, Dursun I, Bakr O M, Brédas J L and Mohammed O F 2017 Molecular behavior of zero-dimensional perovskites *Sci. Adv.* **3** 2–10
[23] Sánchez S, Pfeifer L, Vlachopoulos N and Hagfeldt A 2021 Rapid hybrid perovskite film crystallization from solution *Chem. Soc. Rev.* **50** 7108–31
[24] Dong Q 2015 Electron-hole diffusion lengths >175 μm in solution-grown $CH_3NH_3PbI_3$ single crystals *Science* **347** 967–70
[25] Alcocer M J P, Leijtens T, Herz L M, Petrozza A and Snaith H J 2013 Electron-hole diffusion lengths exceeding trihalide perovskite absorber *Science* **342** 341–4
[26] Zhao D *et al* 2017 Low-bandgap mixed tin-lead iodide perovskite absorbers with long carrier lifetimes for all-perovskite tandem solar cells *Nat. Energy* **2** 1–7
[27] Raja W, de Bastiani M, Allen T G, Aydin E, Razzaq A, ur Rehman A, Ugur E, Babayigit A, Subbiah A S, Isikgor F H and de Wolf S 2021 Photon recycling in perovskite solar cells and its impact on device design *Nanophotonics* **10** 2023–42
[28] van der Laan M *et al* 2021 Photon recycling in $CsPbBr_3$ all-inorganic perovskite nanocrystals *ACS Photonics* **8** 3201–8
[29] Pazos-Outón L M *et al* 2016 Photon recycling in lead iodide perovskite solar cells *Science* **351** 1430–3
[30] Dursun I *et al* 2018 Efficient photon recycling and radiation trapping in cesium lead halide perovskite waveguides *ACS Energy Lett.* **3** 1492–8
[31] Cho C, Zhao B, Tainter G D, Lee J Y, Friend R H, Di D, Deschler F and Greenham N C 2020 The role of photon recycling in perovskite light-emitting diodes *Nat. Commun.* **11** 1–8
[32] Mao W *et al* 2017 Controlled growth of monocrystalline organo-lead halide perovskite and its application in photonic devices *Angew. Chemie - Int. Ed.* **56** 12486–91
[33] Behera T, Pathoor N, Phadnis C, Buragohain S and Chowdhury A 2020 Spatially correlated photoluminescence blinking and flickering of hybrid-halide perovskite micro-rods *J. Lumin.* **223** 117202
[34] Yuan H, Debroye E, Bladt E, Lu G, Keshavarz M, Janssen K P F, Roeffaers M B J, Bals S, Sargent E H and Hofkens J 2018

Imaging heterogeneously distributed photo-active traps in perovskite single crystals *Adv. Mater.* **30** 1–9
[35] Pathoor N, Halder A, Mukherjee A, Mahato J, Sarkar S K and Chowdhury A 2018 Fluorescence blinking beyond nanoconfinement: spatially synchronous intermittency of entire perovskite microcrystals *Angew. Chemie - Int. Ed.* **57** 11603–7
[36] Pathoor N, Mukherjee A and Chowdhury A 2022 Investigating spatiotemporal correlation of multi-state photoluminescence intermittency in organo-lead bromide microcrystal films *J. Phys. Chem.* C **126** 5991–9
[37] Leijtens T, Eperon G E, Noel N K, Habisreutinger S N, Petrozza A and Snaith H J 2015 Stability of metal halide perovskite solar cells *Adv. Energy Mater.* **5** 1–23
[38] Chen R, Xia B, Zhou W, Zhang G, Qin C, Hu J, Scheblykin I G and Xiao L 2022 Environment-dependent metastable nonradiative recombination centers in perovskites revealed by photoluminescence blinking *Adv. Photonics Res.* **3** 2100271
[39] Xu R-P, Li Y-Q, Jin T-Y, Liu Y-Q, Bao Q-Y, O'Carroll C and Tang J-X 2018 *In situ* observation of light illumination-induced degradation in organometal mixed-halide perovskite films *ACS Appl. Mater. Interfaces* **10** 6737–46
[40] Shaw P E, Ruseckas A and Samuel I D W 2008 Exciton diffusion measurements in poly(3-hexylthiophene) *Adv. Mater.* **20** 3516–20
[41] Zhumekenov A A *et al* 2016 Formamidinium lead halide perovskite crystals with unprecedented long carrier dynamics and diffusion length *ACS Energy Lett.* **1** 32–7
[42] Hutter E M, Eperon G E, Stranks S D and Savenije T J 2015 Charge carriers in planar and meso-structured organic-inorganic perovskites: mobilities, lifetimes, and concentrations of trap states *J. Phys. Chem. Lett.* **6** 3082–90
[43] Guo Z, Wan Y, Yang M, Snaider J, Zhu K and Huang L 2017 Long-range hot-carrier transport in hybrid perovskites visualized by ultrafast microscopy *Science* **356** 59–62
[44] Akselrod G M, Deotare P B, Thompson N J, Lee J, Tisdale W A, Baldo M A, Menon V M and Bulovic V 2014 Visualization of exciton transport in ordered and disordered molecular solids *Nat. Commun.* **5** 1–8
[45] He X, Liu P, Wu S, Liao Q, Yao J and Fu H 2017 Multi-color perovskite nanowire lasers through kinetically controlled solution growth followed by gas-phase halide exchange *J. Mater. Chem.* C **5** 12707–13
[46] De S, Layek A, Raja A, Kadir A, Gokhale M R, Bhattacharya A, Dhar S and Chowdhury A 2011 Two distinct origins of highly localized luminescent centers within InGaN/GaN quantum-well light-emitting diodes *Adv. Funct. Mater.* **21** 3828–35
[47] Schneider C A, Rasband W S and Eliceiri K W 2012 NIH Image to ImageJ: 25 years of image analysis *Nat. Methods* **9** 671–5
[48] Jin H, Debroye E, Keshavarz M, Scheblykin I G, Roeffaers M B J, Hofkens J and Steele J A 2020 It's a trap! on the nature of localised states and charge trapping in lead halide perovskites *Mater. Horizons* **7** 397–410
[49] Clark K A, Krueger E L and Vanden Bout D A 2014 Direct measurement of energy migration in supramolecular carbocyanine dye nanotubes *J. Phys. Chem. Lett.* **5** 2274–81
[50] Chen X, Lu H, Yang Y and Beard M C 2018 Excitonic effects in methylammonium lead halide perovskites *J. Phys. Chem. Lett.* **9** 2595–603
[51] Wang Z *et al* 2016 Wavelength-tunable waveguides based on polycrystalline organic-inorganic perovskite microwires *Nanoscale* **8** 6258–64
[52] Oksenberg E, Fai C, Scheblykin I G, Joselevich E, Unger E L, Unold T, Hages C and Merdasa A 2021 Deconvoluting energy transport mechanisms in metal halide perovskites using $CsPbBr_3$ nanowires as a model system *Adv. Funct. Mater.* **31** 2010704
[53] Mohan V and Jain P K 2017 Spectral heterogeneity of hybrid lead halide perovskites demystified by spatially resolved emission *J. Phys. Chem.* C **121** 19392–400